



Summer 7-2020

## Ionic Liquid-Directed Nanoporous TiNb<sub>2</sub>O<sub>7</sub> Anodes with Superior Performance for Fast-Rechargeable Lithium-Ion Batteries

RUNMING TAO

University of Tennessee, Knoxville, RTA03@VOLS.UTK.EDU

University of Tennessee, Knoxville

Follow this and additional works at: [https://trace.tennessee.edu/utk\\_chempubs](https://trace.tennessee.edu/utk_chempubs)

 Part of the [Materials Chemistry Commons](#)

---

### Recommended Citation

TAO, RUNMING and University of Tennessee, Knoxville, "Ionic Liquid-Directed Nanoporous TiNb<sub>2</sub>O<sub>7</sub> Anodes with Superior Performance for Fast-Rechargeable Lithium-Ion Batteries" (2020). *Chemistry Publications and Other Works*.

[https://trace.tennessee.edu/utk\\_chempubs/64](https://trace.tennessee.edu/utk_chempubs/64)

This Article is brought to you for free and open access by the Chemistry at TRACE: Tennessee Research and Creative Exchange. It has been accepted for inclusion in Chemistry Publications and Other Works by an authorized administrator of TRACE: Tennessee Research and Creative Exchange. For more information, please contact [trace@utk.edu](mailto:trace@utk.edu).

# Ionic Liquid-Directed Nanoporous $\text{TiNb}_2\text{O}_7$ Anodes with Superior Performance for Fast-Rechargeable Lithium-Ion Batteries

Runming Tao, Guang Yang, Ethan C. Self, Jiyuan Liang, John R. Dunlap, Shuang Men, Chi-Linh Do-Thanh, Jixing Liu, Yiman Zhang, Sheng Zhao, Hailong Lyu, Alexei P. Sokolov, Jagjit Nanda, Xiao-Guang Sun, and Sheng Dai\*

Nanoporous  $\text{TiNb}_2\text{O}_7$  (NPTNO) material is synthesized by a sol-gel method with an ionic liquid (IL) as the nanoporous structure directing template. NPTNO exhibits a high reversible capacity of  $210 \text{ mAh g}^{-1}$  even at the charging rate of 50 C and an excellent cyclability of half-cell capacity retention of 74% for 1000 cycles at 5 C and  $\text{LiNi}_{0.5}\text{Mn}_{1.5}\text{O}_4$ -coupled full-cell capacity retentions of 81% and 87% for 1000 cycles at 1 C and 2 C, respectively. The studies of the 1000 cycled NPTNO electrode illustrate that the IL-directed mesoporous structure can enhance the cyclability of NPTNO cells due to the alleviation of repetitive mechanical stress and volume fluctuation induced by the repetitive  $\text{Li}^+$  insertion-extraction processes. The measured  $\text{Li}^+$  diffusion coefficients from the galvanostatic intermittent titration technique suggest that the IL-templating strategy indeed ensures the fast rechargeability of NPTNO cells based on the fast  $\text{Li}^+$  diffusion kinetics. Benefiting from the nanoporous structure, NPTNO with unhindered  $\text{Li}^+$  diffusion pathways achieves a superior rate capability in the titanium-based oxide materials and the best full-cell cyclability in the TNO materials. Therefore, the templating potential of IL is demonstrated, and the superb electrochemical performance establishes the IL-directed NPTNO as a promising anode candidate for fast-rechargeable LIBs.

reduction of  $\text{CO}_2$  emissions from diesel and gasoline vehicles.<sup>[1]</sup> However, safety concerns and the lack of high energy storage capacities, excellent cycle life, and fast rechargeabilities deeply impede the future practical applications of LIBs in EVs. An essential challenge has been exploring to find a suitable anode material. Two of the most widely used anode materials in commercial LIB applications are graphite and spinel  $\text{Li}_4\text{Ti}_5\text{O}_{12}$  (LTO). Graphite has excellent structural stability and a high theoretical specific capacity of  $372 \text{ mAh g}^{-1}$ ; however, the safety concerns of solid electrolyte interface (SEI) due to its low operating potential of 0.1 V versus  $\text{Li}/\text{Li}^+$  and low  $\text{Li}^+$  diffusivity have deeply hampered its future in fast-charging applications.<sup>[2-6]</sup> Over the past decade, LTO without SEI issue was considered to be a promising material due to its high operating potential (1.55 V vs  $\text{Li}/\text{Li}^+$ ) and zero-strain property together with superior rate capability and excellent cycle


Lithium-ion batteries (LIBs), recognized as a promising power source of electric vehicles (EVs), are the answer to the increasing global warming issues for their contribution to the

life; however, its future development is dramatically restricted because of its low specific capacity (about  $160 \text{ mAh g}^{-1}$ ).<sup>[3,6-8]</sup> Thus, developing a promising anode material with superior rate capability, high capacity, excellent cycle life, and reliable safety is the key to the future fast-rechargeable LIBs.

R. Tao, Prof. J. Liang, Dr. C.-L. Do-Thanh, Prof. J. Liu, S. Zhao, Dr. H. Lyu, Prof. A. P. Sokolov, Prof. S. Dai  
Department of Chemistry  
University of Tennessee  
Knoxville, TN 37996, USA  
E-mail: dais@ornl.gov

R. Tao, Dr. G. Yang, Dr. E. C. Self, Prof. S. Men, Dr. Y. Zhang, S. Zhao, Dr. H. Lyu, Prof. J. Nanda, Dr. X.-G. Sun, Prof. S. Dai  
Chemical Sciences Division  
Oak Ridge National Laboratory  
Oak Ridge, TN 37830, USA

Dr. J. R. Dunlap  
Joint Institute for Advanced Materials Microscopy Center  
University of Tennessee  
Knoxville, TN 37996, USA

 The ORCID identification number(s) for the author(s) of this article can be found under <https://doi.org/10.1002/sml.202001884>.

In 2011, Goodenough and co-workers proposed that  $\text{TiNb}_2\text{O}_7$  (TNO) with three promising redox couples ( $\text{Ti}^{+4}/\text{Ti}^{+3}$ ,  $\text{Nb}^{+5}/\text{Nb}^{+4}$ , and  $\text{Nb}^{+4}/\text{Nb}^{+3}$ ) could achieve a high specific capacity of  $388 \text{ mAh g}^{-1}$ .<sup>[2,5,9]</sup> TNO's operating voltage of 1.66 V versus  $\text{Li}/\text{Li}^+$  is sufficiently high to avoid the SEI issues and to enhance the safety.<sup>[5,10]</sup> TNO's structural integrity with intercalated  $\text{Li}^+$  is well-maintained by its layered monoclinic structure based on the metal-oxygen octahedra.<sup>[11-13]</sup> Although TNO with some promising electrochemical properties has been regarded as a leading substitute candidate for LTO for the next-generation anode, other characteristics have impeded its application in commercial LIBs.

Like any other metal oxide, TNO suffers from intrinsic electrochemical kinetic issues of poor electrical and ionic conductivities, which vastly limit its future practical applications.<sup>[5,14]</sup> Discovering a way to overcome the electrochemical kinetic

DOI: 10.1002/sml.202001884

limitations of TNO will be the key to fast rechargeability. The rate capability of TNO material highly relies on the solid phase  $\text{Li}^+$  diffusion coefficients, which are, therefore, recognized as an important kinetic characteristic of  $\text{Li}^+$  insertion–extraction. One effective strategy of enhancing the electrochemical kinetics of TNO material is to shorten the  $\text{Li}^+$  diffusion distance by nano-sizing the material to significantly reduce the  $\text{Li}^+$  diffusion time  $t$ , which is proportional to  $L^2/D$ , where  $L$  and  $D$  are the  $\text{Li}^+$  diffusion length and the  $\text{Li}^+$  diffusion coefficient in solid material, respectively.<sup>[5,15,16]</sup> Meanwhile, another strategy for improving the  $\text{Li}^+$  diffusion efficiency is to increase the electrode–electrolyte contact area by introducing porosity.<sup>[14]</sup> Because  $D$  depends on the structure of the material,<sup>[17]</sup> the large open surface area induced by porous structure can enhance the  $\text{Li}^+$  diffusion kinetics. Additionally, porosity can minimize the material's volume fluctuation during the repetitive charge–discharge processes since porous structure contains extra free space to relieve the structural strain from  $\text{Li}^+$  insertion–extraction and to maintain the mechanical stability and structure integrity.<sup>[5,18–20]</sup> Based on those strategies above, unlike bulk TNO (BTNO), nanoporous TNO (NPTNO) has numerous “highways” for  $\text{Li}^+$  diffusion with a greatly improved rate capability and an excellent cycle life.

Although TNO can be synthesized using mechanochemical approaches, the involved ball milling and high temperature treatment cause several disadvantages, such as heterogeneous morphology, large particle size, and low surface area, which lead to poor rate capability.<sup>[12,21]</sup> Zhang and co-workers prepared nano-TNO by solvothermal method,<sup>[22]</sup> but the preparation was too complicated and time consuming.<sup>[14]</sup> To avoid the aforementioned disadvantages, our group once synthesized NPTNO by applying a block copolymer assisted sol-gel method.<sup>[5]</sup> However, the block copolymer assisted preparation was unsuitable for future large-scale industrial production because of the safety concerns of huge volume expansion during calcination and the large environment-unfriendly  $\text{CO}_2$  emissions from polymer burning.<sup>[5,23,24]</sup> The need for a facile and eco-friendly NPTNO synthesis motivated us to explore novel alternative preparation methods.

The distinctive properties of ionic liquids (ILs), namely, negligible volatility and versatile solvation, enable them to be employed in various fields, such as being solvents and/or templates in material synthesis and electrolytes in energy storage devices.<sup>[25–40]</sup> In 1999, our group successfully extended the applications of ILs in the synthesis of porous materials.<sup>[29]</sup> Zhou et al. prepared mesoporous silica by using 1-butyl-3-methylimidazolium ( $[\text{BMIm}]^+$ )-based ILs as porous structure directing templates, and their study proposed the mechanisms of the ILs anions-precursors hydrogen bonding and the neighboring imidazolium rings'  $\pi$ - $\pi$  stacking responsible for the formation of mesoporous oxide frameworks.<sup>[41]</sup> In addition to ILs' application of porous structure templating potential in porous silica synthesis, ILs also can be served in the synthesis of various porous materials. Our group employed ILs as porous structure directing templates to synthesize porous carbonaceous and metal oxides.<sup>[25,33,42–47]</sup> More interestingly, in the IL-templated synthesis of porous metal oxide, the sol-gel hydrolysis and polycondensation of metal precursors can be assisted on the surface of IL “supermolecular” networks.<sup>[29,42]</sup>

Inspired by the prior work above and with the avoidance of employing a block polymer as the porous structure directing template, we postulated that a  $[\text{BMIm}]^+$ -based IL could provide a viable approach to synthesize NPTNO as a promising anode material for LIBs. Since IL can be easily removed and extracted by organic solvents,<sup>[48,49]</sup> this approach holds great potential.

Herein, we report a facile and novel synthesis method based on applying an IL as the structure directing template to fabricate fast-rechargeable NPTNO anode material for LIBs, in which the templating potential of ILs in battery material synthesis is initiated and demonstrated. The obtained NPTNO with fast rechargeability, high specific capacity, and excellent cycle life is recognized as a promising candidate for next-generation LIBs anode material, and the galvanostatic intermittent titration technique (GITT) studies demonstrate that the superior battery performance is mainly due to the enhanced  $\text{Li}^+$  diffusion kinetics via the short  $\text{Li}^+$  diffusion distance and the large contact area between NPTNO and electrolytes.

The NPTNO materials' synthesis schematic diagram is presented in **Figure 1a**. In a typical synthesis, titanium (IV) *n*-butoxide ( $\text{Ti}(\text{O}i\text{Bu})_4$ ) and niobium (V) chloride ( $\text{NbCl}_5$ ) were employed as the starting materials, and IL  $[\text{BMIm}][\text{NTf}_2]$  was applied as the nanoporous structure directing template. The final products were air-calcinated at desired temperatures (more details can be found in the Supporting Information).

**Figure 1b** and **Figure S9**, Supporting Information, show the X-ray diffraction (XRD) patterns of NPTNO materials annealed at different temperatures. The observed diffraction patterns conform to the standard XRD pattern (JCPDS #77-1374). The characteristic diffraction peaks of (002), (110), (003), (−602), and (−512) are ascribed to the  $\text{ReO}_3$ -type structure and have the space group of  $C2/m$  with lattice parameters of  $a = 20.351 \text{ \AA}$ ,  $b = 3.801 \text{ \AA}$ ,  $c = 11.882 \text{ \AA}$ ,  $\alpha = 90.0^\circ$ ,  $\beta = 120.19^\circ$ , and  $\gamma = 90.0^\circ$ .<sup>[13,50]</sup> The obtained crystal structures of NPTNOs belong to monoclinic system with prismatic shape and have the point group of  $C_{2h}$ .<sup>[5,12,13]</sup> The XRD patterns suggest that TNO850 has a higher crystallinity than TNO700. The estimated crystallite sizes of TNO700 and TNO850 by Scherrer equation are around 17.5 and 25.6 nm, respectively, and the larger crystallite size of TNO850 is attributed to the crystal growth at higher temperature.

**Figure 1c** presents the Raman spectra of NPTNO materials in the range between 100 and  $1100 \text{ cm}^{-1}$ . The two characteristic peaks at 1005 and  $901 \text{ cm}^{-1}$  are assigned to the metal–oxygen stretching of edge/corner-shared  $\text{NbO}_6$  octahedra, respectively.<sup>[51]</sup> The three peaks at 650, 535, and  $398 \text{ cm}^{-1}$  are ascribed to the metal–oxygen stretching of  $\text{TiO}_6$  octahedra.<sup>[51,52]</sup> The peaks around  $274 \text{ cm}^{-1}$  are attributed to the symmetric and antisymmetric bending vibrations of O–Ti–O and O–Nb–O.<sup>[51]</sup> The peak at  $147 \text{ cm}^{-1}$  belongs to the external models based on the cation–oxygen stretching.<sup>[51,53,54]</sup> The relatively higher intensities of TNO850 than those of TNO700 indicate higher crystallinity of the former, consistent with their XRD patterns.

**Figure 1d** and **Figure S11**, Supporting Information, display the nitrogen adsorption-desorption isotherms Brunauer–Emmett–Teller (BET) plots of different thermally treated NPTNO materials, respectively. The featured BET plots conform to the IUPAC H4 type loops, which demonstrate the as-synthesized NPTNO materials' internal porosity with 3D

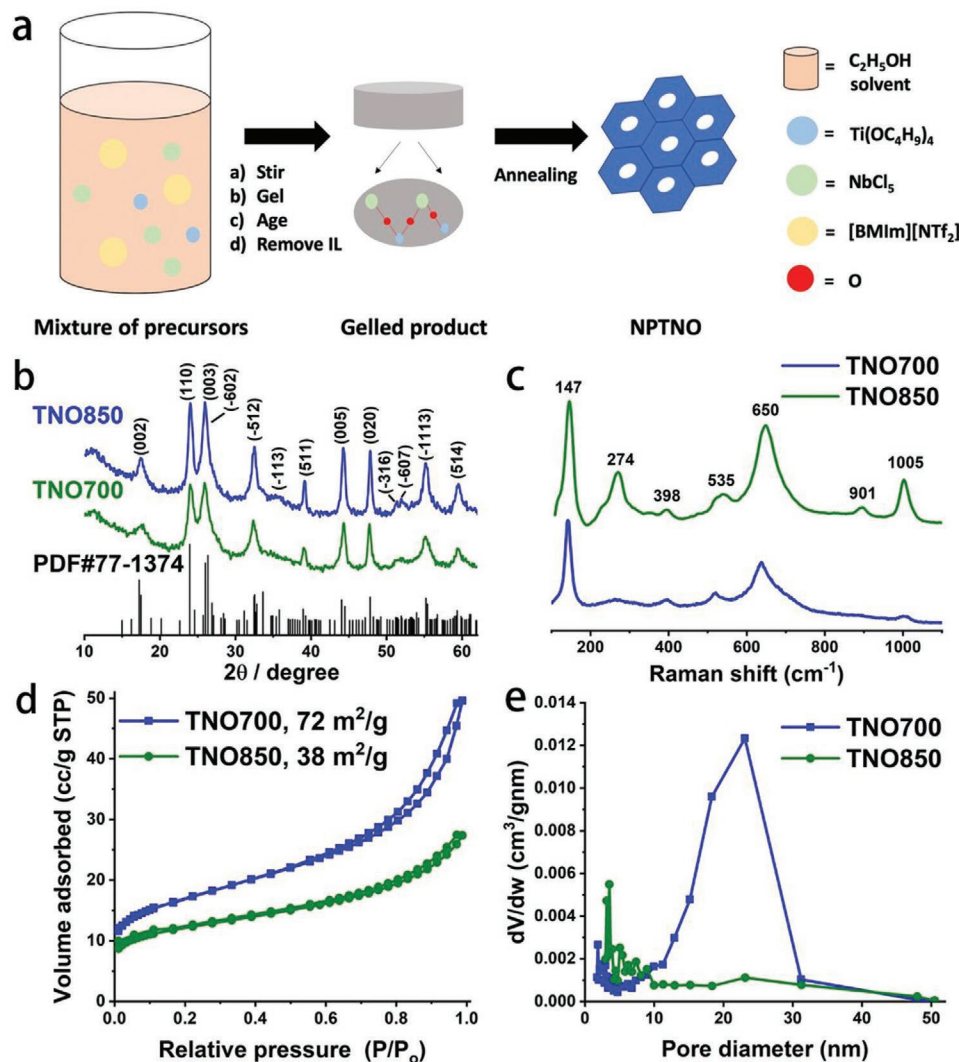


**Figure 1.** Synthesis schematic diagram and structural characterizations of NPTNO materials. a) Synthesis scheme of NPTNO by applying IL as the nanoporous structure-directing template. b) XRD patterns of two NPTNO materials from different calcination temperatures (700 and 850 °C). c) Raman spectra of 700 and 850 °C calcinated NPTNO materials. d,e) Nitrogen adsorption-desorption isotherms BET curves and BJH plots of 700 and 850 °C calcinated NPTNO materials, respectively.

intercrystalline mesopores.<sup>[55]</sup> As a result, the TNO700 and TNO850 materials have high specific surface area of 72 and 38 m<sup>2</sup> g<sup>-1</sup>, respectively. Figure 1e and Figure S12, Supporting Information, show the Barrett–Joyner–Halenda (BJH) pore size distribution plots, demonstrating the presence of a main pore size distribution of 23.1 nm. The pores are formed from the occupied space of the IL template due to the IL anions-precursors hydrogen bonding effects and the neighboring imidazolium rings'  $\pi$ - $\pi$  stack interactions.<sup>[41]</sup>

Transmission electron microscopy (TEM) and scanning electron microscopy (SEM) were employed to further study the morphology and microstructure of the obtained NPTNO materials. **Figure 2** illustrates that TNO700 and TNO850 are composed of nano-intercrystalline mesoporous frameworks, which conform to the BET curves and the BJH plots in Figure 1d,e. In Figure 2a,c, the measured average crystallite sizes of TNO700 and TNO850 are about 18.4 and 29.2 nm,

respectively, which are also similar to those estimated crystallite sizes from XRD patterns. As expected, the observed crystallite size of TNO850 is larger than that of TNO700 due to the crystal growth during the higher-temperature calcination. The selected area electron diffraction patterns in Figure S16, Supporting Information, further indicate that TNO850 has a higher crystallinity than TNO700, which is consistent with the measured XRD patterns above. As shown in Figure 2b,d, the measured d-spacings of 0.370 and 0.341 nm correspond to the (110) and (003) crystallographic planes, respectively. As shown in Figure S15a,c, Supporting Information, the SEM images of the synthesized NPTNO materials present 3D porous structure, which ensures high contact area between electrolytes and electrode to benefit the Li<sup>+</sup> diffusion. Moreover, the SEM element mapping reveals an even element distribution of Ti, Nb, and O in the NPTNO materials (Figure S15b,d, Supporting Information).

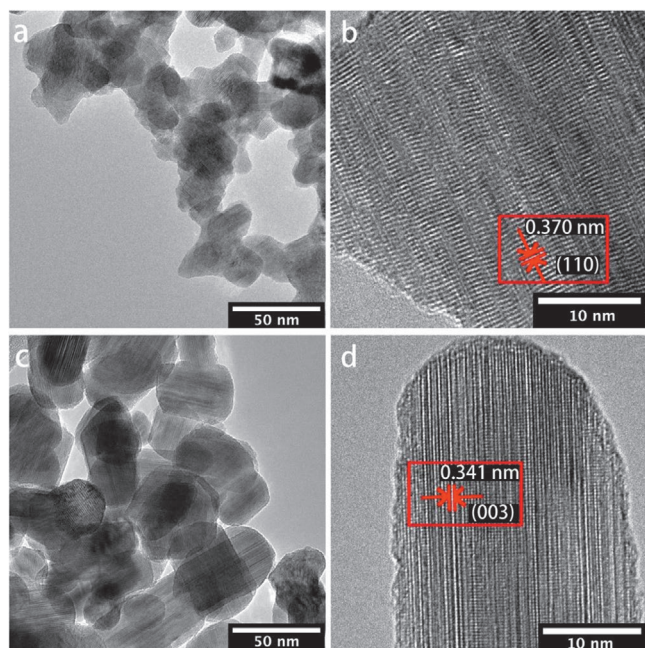


**Figure 2.** TEM images of the obtained NPTNO materials at different magnifications. a,b) TNO700. c,d) TNO850.

To investigate the electrochemical performance of the synthesized NPTNO materials, coin cells were assembled with Li metal as the counter electrodes. All the assembled half-cells were cycled in the range of 1.0–3.0 V. **Figure 3a** shows the cyclic voltammetry (CV) curves of TNO700 based half-cell at a scan rate of 0.05 mV s<sup>-1</sup>. The sharp redox peaks at about 1.60 and 1.72 V are attributed to Nb<sup>5+</sup>/Nb<sup>4+</sup> redox couple and the small peaks at around 1.73 and 2.00 V to the Ti<sup>4+</sup>/Ti<sup>3+</sup> redox pair.<sup>[13,22,55]</sup> The difference of reduction peak position between the first cycle and the following cycles is due to Fermi level migration and metal–oxygen octahedra distortion during the Li<sup>+</sup> insertion.<sup>[12,13,55]</sup> In addition, the overlapped CV profiles after the first cycle indicate the NPTNO anode's excellent electrochemical and cycling stability.<sup>[55]</sup>

**Figure 3b** shows the galvanostatic discharge–charge curves of nanoporous TNO700 half-cell at a current rate of 0.1 C (38.7 mA g<sup>-1</sup>). A reversible capacity of 281 mAh g<sup>-1</sup> is obtained, and the overall discharge plateau of NPTNO materials occurs at 1.66 V. For TNO700, the initial discharge (Li insertion) and charge (Li extraction) capacities are 316 and 276 mAh g<sup>-1</sup> with a Coulombic efficiency of 87.7%. For TNO850, the initial discharge and charge capacities are 306 and 279 mAh g<sup>-1</sup> with a Coulombic efficiency of 91.1% (**Figure S19b**, Supporting Information). For comparison, the initial cycle's discharge, charge capacities, and calculated Coulombic efficiency of BTNO are 325, 302 mAh g<sup>-1</sup> and 93.0%, respectively (**Figure S19d**, Supporting Information). All the aforementioned reversible capacities of the TNO materials are above 275 mAh g<sup>-1</sup>, which is distinctively higher than that of LTO, and it is almost comparable to some commercial graphite anodes (300–330 mAh g<sup>-1</sup>).<sup>[5,56]</sup> In addition, the higher irreversible capacities of NPTNO materials mainly stem from the potential side reactions between electrolytes and NPTNO's numerous active sites on the large surface, which can lower the initial Coulombic efficiency.<sup>[12,57]</sup>

To demonstrate the fast rechargeability of the IL-templated NPTNO materials, multiple C rates within the range of 0.5–50 C were assessed on the assembled half cells. As shown in **Figure 3c**, TNO700 exhibits the best rate capability, and its average reversible discharge capacities over 10 cycles at 10 C, 20 C, and 50 C are 235, 218, and 210 mAh g<sup>-1</sup>, respectively. TNO850's average discharge capacities over 10 cycles at 10 C, 20 C, and 50 C are 209, 203, and 194 mAh g<sup>-1</sup>, correspondingly. The slightly worse rate capability of TNO850 than that of TNO700 can be attributed to the relatively larger particle sizes and relatively lower porosity of TNO850, which are caused by the higher-temperature treatment in the calcination process. For comparison, the average reversible discharge capacities of BTNO over 10 cycles at 10 C, 20 C, and 50 C are 176, 131, and 58 mAh g<sup>-1</sup>, respectively, which are much lower than those of NPTNO materials. Therefore, the distinctively higher reversible discharge capacities of the NPTNO materials than those of BTNO suggest that the nanocrystal-composed mesoporous structure of the former can enhance their rate capabilities.

Besides fast rechargeability, an excellent cycle life is another requirement of future commercial fast-rechargeable LIBs. Impressively, NPTNO exhibits excellent cyclic performances at a high discharge–charge rate of 5 C for 1000 cycles (**Figure 3d**). The reversible capacities of the first cycle and the 1000th cycle of the nanoporous TNO700 half-cell are 243 and 180 mAh g<sup>-1</sup>, respectively, and the calculated capacity retention is 74%. In contrast, due to the low porosity and surface area, the cyclic performance of TNO850 is not as good as that of TNO700, and the obtained reversible capacities of the first and the 1000th cycles of the TNO850 half-cell are 241 and 112 mAh g<sup>-1</sup>, respectively, with a capacity retention of 46%. The NPTNO anodes' low Coulombic efficiency in the first few cycles can be attributed to the side reactions on the large surface area, as discussed previously. In sharp contrast, BTNO's poor 5 C cyclic performance with a capacity retention of 28% can not fulfill the practical requirements. Unlike BTNO suffering from volume fluctuation, NPTNO anodes have the extra free space to relieve the structural strain from Li<sup>+</sup> insertion–extraction and maintain the mechanical stability and structural integrity, leading to remarkable excellent cycling stability.<sup>[5,18–20]</sup>

To further demonstrate NPTNO's practical application, LiNi<sub>0.5</sub>Mn<sub>1.5</sub>O<sub>4</sub> (LNMO) cathode paired full-cell study was investigated in voltage range from 1.5 to 3.5 V. **Figure 3e** shows the LNMO-TNO700 full-cell galvanostatic charge–discharge curves at 2 C, and a reversible capacity of 203 mAh g<sup>-1</sup> is obtained. The full-cell system's operating voltage is about 3.0 V. **Figure 3f** displays the cyclic performance of TNO700 at 2 C over 1000 cycles, and its excellent capacity retention is 87% with Coulombic efficiency of nearly 99.9%. The obtained cyclic performance of the IL-templated TNO700 at 2 C over 1000 cycles is comparable to that of our group's previous copolymer-directed NPTNO at 1 C (a reversible capacity of 220 mAh g<sup>-1</sup> with a capacity retention of 82% over 1000 cycles).<sup>[5]</sup> **Figure S20**, Supporting Information, shows the battery performance of LNMO-TNO700 full-cell at a lower current rate of 1 C. A reversible capacity of 252 mAh g<sup>-1</sup> is observed, and the obtained capacity retention over 1000 cycles is about 81% with Coulombic efficiency of around 99.9%. To the best of our knowledge, the IL-templated NPTNO materials exhibit the best full-cell cyclic performance

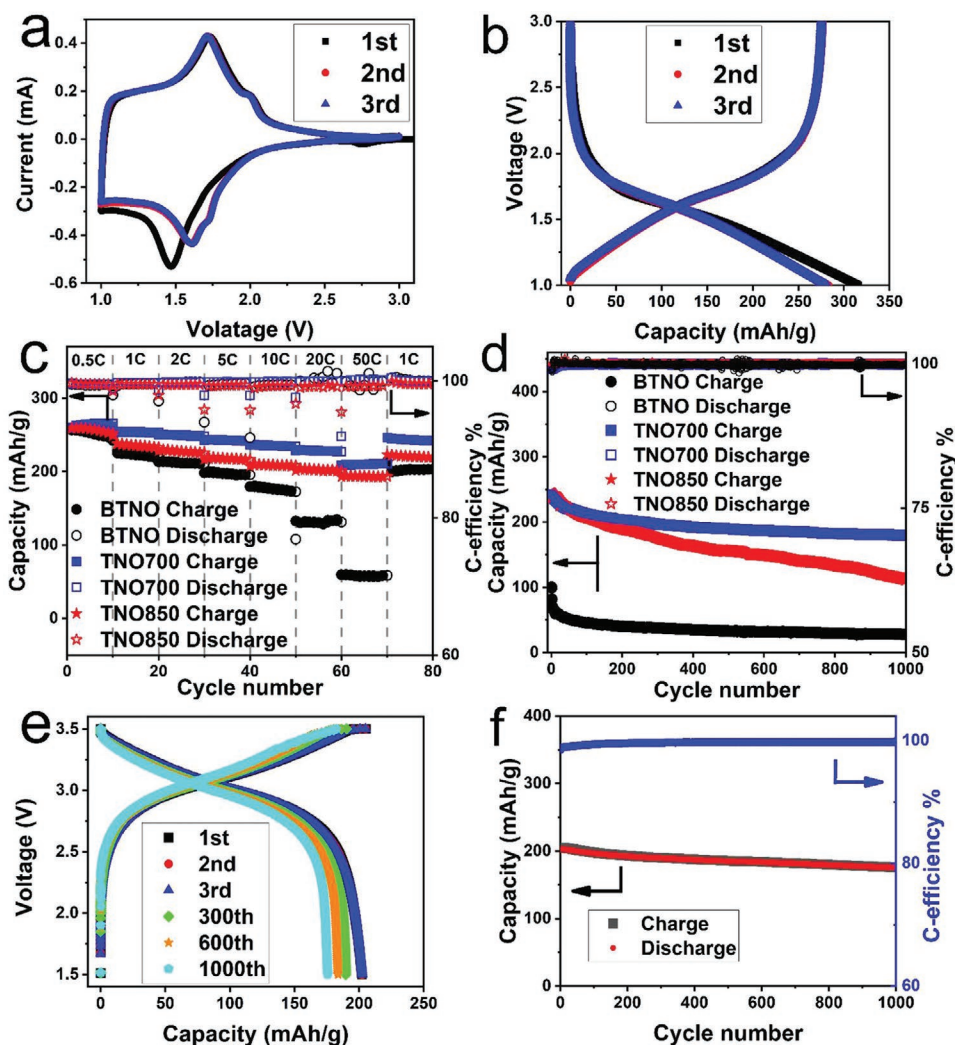


**Figure 3.** Electrochemical characterizations of the obtained NPTNO anodes. a) Cyclic voltammograms of TNO700 half-cell at a scan rate of  $0.05 \text{ mV s}^{-1}$ . b)  $0.1 \text{ C}$  galvanostatic discharge–charge plots of TNO700 half-cell. c) Rate capability and Coulombic efficiency comparisons between NPTNO half-cells and BTNO half-cell at various rates with discharge current rate fixed at  $1 \text{ C}$  (except the  $0.5 \text{ C}$  discharge–charge profile). d) Cyclic performance and Coulombic efficiency comparisons between NPTNO half-cells and BTNO half-cell at  $5 \text{ C}$  after  $0.1 \text{ C}$  aging for three cycles. e, f) Galvanostatic and cyclic performance charge–discharge curves of LNMO-TNO700 full-cell at  $2 \text{ C}$  (after aging at  $0.1 \text{ C}$  for five cycles).

in the TNO materials. Thereby, the above excellent battery performance of the LNMO-TNO700 full-cells illustrates that the IL-templated NPTNO material indeed holds great potential for future practical applications.

To investigate the stability of TNO700 during the battery cycling, the 1000 cycled TNO700 half-cell was disassembled and characterized. **Figure 4a** shows that the TNO700 electrode after 1000 cycles shares the same XRD patterns as those of the pristine TNO700 material, indicating the crystal structural stability and robustness of the IL-templated NPTNO material.<sup>[12]</sup> The SEM images in **Figure S18**, Supporting Information, reveal that the pristine and the 1000 cycled electrodes share the same morphology, demonstrating the structural integrity of the TNO700 material. In addition, the similar broad X-ray photoelectron spectroscopy (XPS) spectra of the uncycled and the 1000 cycled TNO700 electrodes in **Figure 4b** confirm the existences of Ti, Nb, O, C, and F, which is consistent with

the SEM element mapping results in **Figure S18d**, Supporting Information. The high-resolution XPS (HRXPS) spectra of the Ti and Nb elements in **Figure S21a,b**, Supporting Information, are similar to those in **Figure S21c,d**, Supporting Information, reflecting the excellent electrochemical stability of TNO700 material over 1000 cycles.<sup>[13,58–61]</sup> In consideration of the potential side reactions during the cycling, the HRXPS of C, O and F elements is also acquired, as shown in **Figure 4c,d**. Some obvious changes on the HRXPS of C, O, and F elements are observed, confirming the existence of side reactions. On the C HPXPS of 1000 cycled TNO700 electrode in **Figure 4d**, the peaks at  $287.8$  and  $286.2 \text{ eV}$  are assigned to C=O group and C–OH/C–O–C groups,<sup>[62,63]</sup> which are due to the decomposition of carbonates during the cycling. Those aforementioned groups are also apparent on the O HRXPS of the 1000 cycled electrode,<sup>[13,64–66]</sup> revealing the decomposition of carbonates. Additionally, the presence of LiF peak at

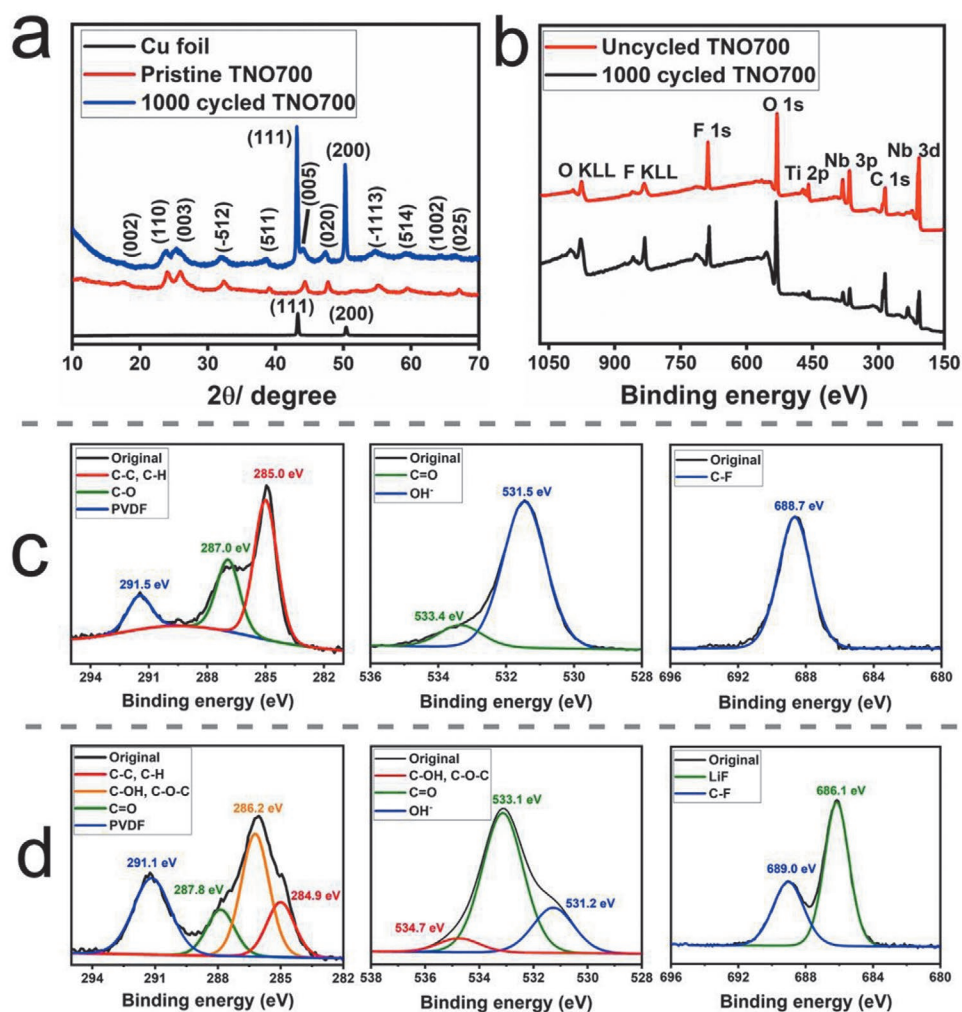


**Figure 4.** Studies of half-cell long-term cycled TNO700's structural change. a) XRD patterns of pristine TNO700 powder and the 1000 cycled TNO700 electrode at charge state. b) XPS broad spectra of the uncycled and the 1000 cycled TNO700 electrodes at charge state. c) The HRXPS of C, O, and F elements for the uncycled TNO700 electrode. d) The HRXPS of C, O, and F elements for the 1000 cycled TNO700 electrode.

686.1 eV on the F HRXPS can be attributed to the side reaction of  $\text{LiPF}_6$  salt.<sup>[67]</sup>

To further understand the excellent rate performance of the NPTNO materials, GITT studies were carried out to measure the  $\text{Li}^+$  diffusion coefficients. The apparent  $\text{Li}^+$  diffusion coefficients of TNO anodes are calculated by the following equation derived from Fick's second law<sup>[21,62]</sup>

$$D = \frac{4}{\pi\tau} \left( \frac{n_m V_m}{S} \right)^2 \left( \frac{\Delta E_s}{\Delta E_t} \right)^2 \quad (1)$$

where  $D$  is the  $\text{Li}^+$  diffusion coefficient,  $\tau$  is the duration of the current pulse (s),  $n_m$  is the number of moles (mol),  $V_m$  is the molar volume of the active material ( $\text{cm}^3 \text{mol}^{-1}$ ),  $S$  is the electrode-electrolyte contact area ( $\text{cm}^2$ ),  $\Delta E_s$  is the equilibrium voltage change induced by current pulse; and  $\Delta E_t$  is the voltage change during the constant current pulse (neglecting the  $iR$  drop). **Figure 5a** presents the measured GITT profiles of the three TNO electrodes during galvanostatic discharge–charge process, and the obtained similar potential plateaus are due

to the same variation of TNO crystal structures during the  $\text{Li}^+$  insertion–extraction. The inset of **Figure 5a** shows two typical discharge steps for the TNO700 half-cell, in which the cell potential quickly decreases due to the  $iR$  drop, followed by a relatively slow potential decrease due to the galvanostatic discharge current pulse. While during the relaxation time, the potential immediately increases due to the  $iR$ , and then slowly increases. The 1 h relaxation after 200 s pulse discharge is long enough to allow the electrode reaching the equilibrium statuses. **Figure 5b** shows the variation of  $\text{Li}^+$  diffusion coefficients changing with voltage during the discharge–charge processes for the NPTNO and BTNO electrodes. During the discharge process, when potential is above 1.70 V, unlike BTNO anode having a stable  $D$  value because of its very little surface area, the  $D$  values' of NPTNO electrodes rapidly decrease due to the quick filling of  $\text{Li}^+$  on their nanocrystal composed mesoporous structures' large surface areas. The decrements of  $D$  values from 1.70 to 1.65 V are ascribed to the transformation from solid-solution phase (SS1) to two-phase coexistence (SS1 and SS2), and the rapid  $D$  value increments from 1.65 to 1.60 V are attributed

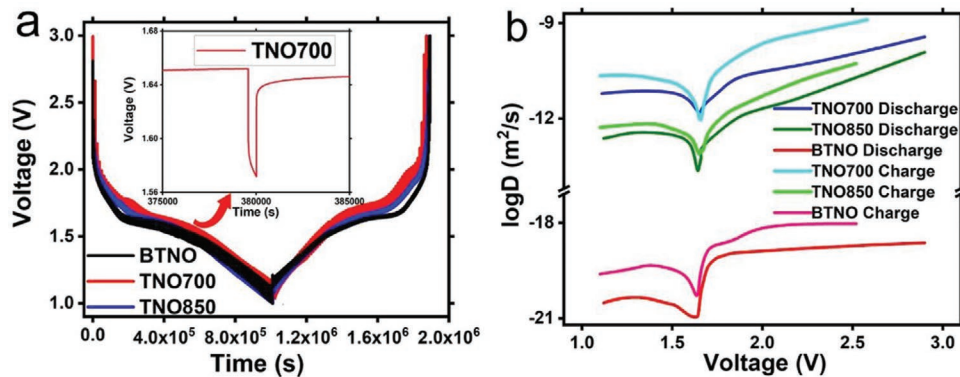


**Figure 5.** GITT  $\text{Li}^+$  diffusivity studies of TNO anodes in half-cells. a) GITT curves of the TNO electrodes. b) GITT  $\text{Li}^+$  insertion-extraction processes' diffusivity plots of TNO anodes based on the BET-reported surface areas.

to the transition from two-phase coexistence (SS1 and SS2) to solid-solution phase (SS2).<sup>[5,21,62]</sup> Then, the  $D$  values stabilize between 1.60 and 1.00 V. The observed  $\text{Li}^+$  diffusion coefficients of the  $\text{Li}^+$  extraction process are generally higher than those of the  $\text{Li}^+$  insertion process. To the best of our knowledge and conjecture, this observation may be attributed to the inflexible volume expansion due to the metal–oxygen octahedra distortion induced by the irreversibly inserted  $\text{Li}^+$  in the crystal lattice, which may also relate to the irreversible capacity decay in the 0.1 C galvanostatic discharge–charge plots and the positional shift of the reduction peaks between the first cycle and following cycles in Figure 3a,b.<sup>[12,13,55]</sup>

As shown in Figure 5b, the  $\text{Li}^+$  diffusion coefficients of NPTNO electrodes are obviously greater than those of BTNO electrode ( $D_{\text{TNO700}} > D_{\text{TNO850}} > D_{\text{BTNO}}$ ), which suggests that the  $\text{Li}^+$  diffusion coefficients of the NPTNO electrodes heavily depend on the nanocrystal and porosity-induced large surface area. As shown in Tables S2 and S3, Supporting Information, the measured  $\text{Li}^+$  diffusion coefficients of the NPTNO materials remarkably surpass those of other  $\text{ReO}_3$ -type  $\text{M-Nb-O}$  anode materials.<sup>[68–73]</sup> According to the relationship of  $t \approx L^2/D$ , the IL-templated NPTNO materials indeed have faster  $\text{Li}^+$  insertion–extraction kinetics than BTNO anode due to the shorter diffusion distance and larger  $\text{Li}^+$  diffusion coefficients induced by the nanocrystal-composed mesoporous structure (Table S2, Supporting Information). To the best of our knowledge, the as-synthesized NPTNO materials exhibit a superior rate capability in the titanium-based oxide materials (Table S4, Supporting Information).

As well-demonstrated in the above results, the utilization of the open and interconnected mesoporous framework composed of TNO nanocrystals can dramatically enhance the overall battery performance of IL-templated NPTNO materials at high rates. First, by virtue of IL-templating strategy, the obtained nanocrystal can enhance the occurring of the electrochemical reactions on the surface and near the surface regions of electrode.<sup>[13,61]</sup> This ensures an unhindered and straightforward  $\text{Li}^+$  insertion–extraction kinetics; thereby, the rate capability is no longer limited by  $\text{Li}^+$  diffusion anymore. Second, the open mesoporous framework with large surface area provides a high contact between electrolytes and electrode, which significantly improves the  $\text{Li}^+$  diffusion pathways.<sup>[5,12]</sup> This further ensures the excellent rate capability. Lastly, the mesoporous structure,

by alleviating the repetitive mechanical stress and volume fluctuation induced by the  $\text{Li}^+$  insertion–extraction processes, enhances the cycle life.<sup>[5,18–20]</sup>

In summary, the NPTNO materials synthesized by using IL as a nanoporous structure directing template dramatically enhance the LIB performance in terms of superior fast rechargeability, high specific capacity, and excellent cycle life. Benefitting from the IL-directed mesoporous structures composed of nanocrystals, the obtained NPTNO achieves a superb fast rechargeability of  $210 \text{ mAh g}^{-1}$  at 50 C and an excellent cycle life of 1000 cycles with capacity retention of 74% at 5 C. The outstanding fast rechargeability of NPTNO materials is due to their dramatically enhanced  $\text{Li}^+$  diffusion coefficients, demonstrated by the GITT measurements. Additionally, the LNMO cathode-coupled full-cells present extraordinary battery performance. The full-cells achieve reversible capacities of 203 and  $252 \text{ mAh g}^{-1}$  with capacity retentions of 81% and 87% for 1000 cycles at 1 C and 2 C, respectively. So far, the IL-directed NPTNO exhibits a highly promising rate capability in the titanium-based oxide materials with the best full-cell cyclic performance in the TNO materials. Such superior electrochemical performance suggests that the IL-templating effect is essential, and the IL-directed NPTNO is a highly promising candidate of anode material that suits the practical application of fast-rechargeable LIBs for EVs.

## Supporting Information

Supporting Information is available from the Wiley Online Library or from the author.

## Acknowledgements

The research at Oak Ridge National Laboratory and the University of Tennessee at Knoxville was supported by the U.S. Department of Energy's Office of Science, Office of Basic Energy Science, Division of Materials Sciences Engineering under contract number DE-AC05-00OR22725. The electron microscopy work was performed at Joint Institute for Advanced Materials Microscopy Center by J.R.D. The X-ray photoelectron spectroscopy analysis was conducted in Oak Ridge National Laboratory by S.M. This manuscript was authored by



UT-Battelle, LLC under contract number DE-AC05-00OR22725 with the U.S. Department of Energy.

## Conflict of Interest

The authors declare no conflict of interest.

## Keywords

fast rechargeabilities, ionic liquid, Li<sup>+</sup> diffusion, LIB anode materials, nanoporous TiNb<sub>2</sub>O<sub>7</sub>

Received: March 22, 2020

Revised: May 7, 2020

Published online: June 22, 2020

- [1] M. M. Thackeray, C. Wolverton, E. D. Isaacs, *Energy Environ. Sci.* **2012**, 5, 7854.
- [2] H. Yu, H. Lan, L. Yan, S. Qian, X. Cheng, H. Zhu, N. Long, M. Shui, J. Shu, *Nano Energy* **2017**, 38, 109.
- [3] T. Shodai, S. Okada, S.-I. Tobishima, J.-I. Yamaki, *Solid State Ionics* **1996**, 86–88, 785.
- [4] J. M. Tarascon, M. Armand, *Nature* **2001**, 414, 359.
- [5] B. Guo, X. Yu, X.-G. Sun, M. Chi, Z.-A. Qiao, J. Liu, Y.-S. Hu, X.-Q. Yang, J. B. Goodenough, S. Dai, *Energy Environ. Sci.* **2014**, 7, 2220.
- [6] J. B. Goodenough, Y. Kim, *Chem. Mater.* **2010**, 22, 587.
- [7] X. Feng, C. Shen, N. Ding, C. Chen, *J. Mater. Chem.* **2012**, 22, 20861.
- [8] K. J. Griffith, I. D. Seymour, M. A. Hope, M. M. Butala, L. K. Lamontagne, M. B. Preefer, C. P. Koçer, G. Henkelman, A. J. Morris, M. J. Cliffe, S. E. Dutton, C. P. Grey, *J. Am. Chem. Soc.* **2019**, 141, 16706.
- [9] J.-T. Han, Y.-H. Huang, J. B. Goodenough, *Chem. Mater.* **2011**, 23, 2027.
- [10] H. Song, Y.-T. Kim, *Chem. Commun.* **2015**, 51, 9849.
- [11] A. D. Wadsley, *Acta Crystallogr.* **1961**, 14, 660.
- [12] X. Lu, Z. Jian, Z. Fang, L. Gu, Y.-S. Hu, W. Chen, Z. Wang, L. Chen, *Energy Environ. Sci.* **2011**, 4, 2638.
- [13] S. Lou, X. Cheng, Y. Zhao, A. Lushington, J. Gao, Q. Li, P. Zuo, B. Wang, Y. Gao, Y. Ma, C. Du, G. Yin, X. Sun, *Nano Energy* **2017**, 34, 15.
- [14] S. Lou, Y. Ma, X. Cheng, J. Gao, Y. Gao, P. Zuo, C. Du, G. Yin, *Chem. Commun.* **2015**, 51, 17293.
- [15] M. D. Levi, D. Aurbach, *J. Phys. Chem. B* **1997**, 101, 4641.
- [16] Y. Ren, A. R. Armstrong, F. Jiao, P. G. Bruce, *J. Am. Chem. Soc.* **2010**, 132, 996.
- [17] L. Pfaffmann, C. Birkenmaier, M. Müller, W. Bauer, T. Mitsch, J. Feinauer, Y. Krämer, F. Scheiba, A. Hintennach, T. Schleid, V. Schmidt, H. Ehrenberg, *J. Power Sources* **2016**, 307, 762.
- [18] Z. Liu, X. Yuan, S. Zhang, J. Wang, Q. Huang, N. Yu, Y. Zhu, L. Fu, F. Wang, Y. Chen, Y. Wu, *NPG Asia Mater.* **2019**, 11, 12.
- [19] H. Zhang, H. Zhao, M. A. Khan, W. Zou, J. Xu, L. Zhang, J. Zhang, *J. Mater. Chem. A* **2018**, 6, 20564.
- [20] H. Choi, P. No, Y.-J. Lee, J.-H. Choi, *J. Appl. Electrochem.* **2017**, 47, 1127.
- [21] R. Inada, R. Kumasaka, S. Inabe, T. Tojo, Y. Sakurai, *J. Electrochem. Soc.* **2019**, 166, A5157.
- [22] H. Li, L. Shen, G. Pang, S. Fang, H. Luo, K. Yang, X. Zhang, *Nanoscale* **2015**, 7, 619.
- [23] Z. Huang, W. Shi, *Polym. Degrad. Stab.* **2007**, 92, 1193.
- [24] T. Kashiwagi, *Symp. (Int.) Combust., [Proc.]* **1994**, 25, 1423.
- [25] Z. Ma, J. Yu, S. Dai, *Adv. Mater.* **2010**, 22, 261.
- [26] H. Zhao, S. Xia, P. Ma, *J. Chem. Tech. Biotechnol.* **2005**, 80, 1089.
- [27] J. Ding, D. Zhou, G. Spinks, G. Wallace, S. Forsyth, M. Forsyth, D. MacFarlane, *Chem. Mater.* **2003**, 15, 2392.
- [28] S. Menne, J. Pires, M. Anouti, A. Balducci, *Electrochem. Commun.* **2013**, 31, 39.
- [29] S. Dai, Y. H. Ju, H. J. Gao, J. S. Lin, S. J. Pennycook, C. E. Barnes, *Chem. Commun.* **2000**, 243.
- [30] X.-G. Sun, S. Dai, *Electrochim. Acta* **2010**, 55, 4618.
- [31] C. Liao, X.-G. Sun, S. Dai, *Electrochim. Acta* **2013**, 87, 889.
- [32] X.-G. Sun, C. Liao, N. Shao, J. R. Bell, B. Guo, H. Luo, D.-E. Jiang, S. Dai, *J. Power Sources* **2013**, 237, 5.
- [33] B. Wang, J. Di, P. Zhang, J. Xia, S. Dai, H. Li, *Appl. Catal., B* **2017**, 206, 127.
- [34] A. Taubert, Z. Li, *Dalton Trans.* **2007**, 723.
- [35] J. Le Bideau, L. Viau, A. Vioux, *Chem. Soc. Rev.* **2011**, 40, 907.
- [36] M. Antonietti, D. Kuang, B. Smarsly, Y. Zhou, *Angew. Chem., Int. Ed.* **2004**, 43, 4988.
- [37] T. Brezesinski, C. Erpen, K.-I. Iimura, B. Smarsly, *Chem. Mater.* **2005**, 17, 1683.
- [38] H. Kaper, S. Sallard, I. Djerdj, M. Antonietti, B. M. Smarsly, *Chem. Mater.* **2010**, 22, 3502.
- [39] P. Voepel, C. Seitz, J. M. Waack, S. Zahn, T. Leichtweiß, A. Zaichenko, D. Mollenhauer, H. Amenitsch, M. Voggenreiter, S. Polarz, B. M. Smarsly, *Cryst. Growth Des.* **2017**, 17, 5586.
- [40] K. Schütte, J. Barthel, M. Endres, M. Siebels, B. M. Smarsly, J. Yue, C. Janiak, *ChemistryOpen* **2017**, 6, 137.
- [41] Y. Zhou, J. H. Schattka, M. Antonietti, *Nano Lett.* **2004**, 4, 477.
- [42] P. Zhang, H. Lu, Y. Zhou, L. Zhang, Z. Wu, S. Yang, H. Shi, Q. Zhu, Y. Chen, S. Dai, *Nat. Commun.* **2015**, 6, 8446.
- [43] X. Zhu, P. C. Hillesheim, S. M. Mahurin, C. Wang, C. Tian, S. Brown, H. Luo, G. M. Veith, K. S. Han, E. W. Hagaman, H. Liu, S. Dai, *ChemSusChem* **2012**, 5, 1912.
- [44] J. S. Lee, X. Wang, H. Luo, G. A. Baker, S. Dai, *J. Am. Chem. Soc.* **2009**, 131, 4596.
- [45] X. Wang, S. Dai, *Angew. Chem., Int. Ed.* **2010**, 49, 6664.
- [46] S. Zhou, Z. Ma, G. A. Baker, A. J. Rondinone, Q. Zhu, H. Luo, Z. Wu, S. Dai, *Langmuir* **2009**, 25, 7229.
- [47] X. Cui, Q. Yang, Y. Xiong, Z. Bao, H. Xing, S. Dai, *Chem. Commun.* **2017**, 53, 4915.
- [48] V. Najdanovic-Visak, L. P. N. Rebelo, M. Nunes da Ponte, *Green Chem.* **2005**, 7, 443.
- [49] A. Chapeaux, L. D. Simoni, T. S. Ronan, M. A. Stadtherr, J. F. Brennecke, *Green Chem.* **2008**, 10, 1301.
- [50] D. Saritha, U. V. Varadaraju, *Mater. Res. Bull.* **2013**, 48, 2702.
- [51] N. G. Eror, U. Balachandran, *J. Solid State Chem.* **1982**, 45, 276.
- [52] W. Wen, J.-M. Wu, Y.-Z. Jiang, L.-L. Lai, J. Song, *Chem* **2017**, 2, 404.
- [53] A. A. McConnell, J. S. Aderson, C. N. R. Rao, *Spectrochim. Acta, Part A* **1976**, 32, 1067.
- [54] C. N. R. Rao, *Indian J. Pure Appl. Phys.* **1978**, 16, 277.
- [55] L. Fei, Y. Xu, X. Wu, Y. Li, P. Xie, S. Deng, S. Smirnov, H. Luo, *Nanoscale* **2013**, 5, 11102.
- [56] R. M. Humana, M. G. Ortiz, J. E. Thomas, S. G. Real, M. Sedlarikova, J. Vondrák, A. Visintin, *ECS Trans.* **2014**, 63, 91.
- [57] J. Xu, R. D. Deshpande, J. Pan, Y.-T. Cheng, V. S. Battaglia, *J. Electrochem. Soc.* **2015**, 162, A2026.
- [58] Y. Luo, J. Luo, J. Jiang, W. Zhou, H. Yang, X. Qi, H. Zhang, H. J. Fan, D. Y. W. Yu, C. M. Li, T. Yu, *Energy Environ. Sci.* **2012**, 5, 6559.
- [59] Z. Jian, X. Lu, Z. Fang, Y.-S. Hu, J. Zhou, W. Chen, L. Chen, *Electrochem. Commun.* **2011**, 13, 1127.
- [60] X. Wang, G. Shen, *Nano Energy* **2015**, 15, 104.
- [61] B. Dunn, *Science* **2014**, 343, 1210.

- [62] K. Ise, S. Morimoto, Y. Harada, N. Takami, *Solid State Ionics* **2018**, 320, 7.
- [63] C. Mattevi, G. Eda, S. Agnoli, S. Miller, K. A. Mkhoyan, O. Celik, D. Mastrogiovanni, G. Granozzi, E. Garfunkel, M. Chhowalla, *Adv. Funct. Mater.* **2009**, 19, 2577.
- [64] R. Al-Gaashani, S. Radiman, A. R. Daud, N. Tabet, Y. Al-Douri, *Ceram. Int.* **2013**, 39, 2283.
- [65] B. Gupta, N. Kumar, K. Panda, V. Kanan, S. Joshi, I. Visoly-Fisher, *Sci. Rep.* **2017**, 7, 45030.
- [66] Y. C. G. Kwan, G. M. Ng, C. H. A. Huan, *Thin Solid Films* **2015**, 590, 40.
- [67] L. Martin, H. Martinez, D. Poinot, B. Pecquenard, F. Le Cras, *J. Power Sources* **2014**, 248, 861.
- [68] L. Yan, H. Lan, H. Yu, S. Qian, X. Cheng, N. Long, R. Zhang, M. Shui, J. Shu, *J. Mater. Chem. A* **2017**, 5, 8972.
- [69] X. Zhu, H. Cao, R. Li, Q. Fu, G. Liang, Y. Chen, L. Luo, C. Lin, X. S. Zhao, *J. Mater. Chem. A* **2019**, 7, 25537.
- [70] X. Zhu, J. Xu, Y. Luo, Q. Fu, G. Liang, L. Luo, Y. Chen, C. Lin, X. S. Zhao, *J. Mater. Chem. A* **2019**, 7, 6522.
- [71] X. Lou, C. Lin, Q. Luo, J. Zhao, B. Wang, J. Li, Q. Shao, X. Guo, N. Wang, Z. Guo, *ChemElectroChem* **2017**, 4, 3171.
- [72] Z. Wang, R. Zheng, Y. Li, H. Yu, J. Zhang, X. Zhang, W. Bi, M. Shui, J. Shu, *Ceram. Int.* **2020**, 46, 5913.
- [73] Q. Fu, X. Liu, J. Hou, Y. Pu, C. Lin, L. Yang, X. Zhu, L. Hu, S. Lin, L. Luo, Y. Chen, *J. Power Sources* **2018**, 397, 231.